

SI Appendix for "Identification of chondritic krypton and xenon in Yellowstone gases and the timing of terrestrial volatile accretion"

Michael W. Broadley, Peter H. Barry, David V. Bekaert David J. Byrne, Antonio Caracausi, Christopher J. Ballentine, Bernard Marty

This PDF file includes:

Supplementary Text

Figures S1 - S10

Tables S1 - S3

References for the SI Appendix

Materials and Methods

All samples collected in Giggenbach bottles were first transferred into evacuated 500 cm³ steel tanks within 2 weeks of collection to avoid significant loss of He by diffusion through the glass walls of the bottle (1). The NaOH solution present within the glass Giggenbach flask traps reactive gases (e.g. H₂O, CO₂, SO₂, HCl, HF), therefore allowing the non-reactive noble gases to be concentrated within the empty headspace. This sampling method drastically increases the amount of gas available for analysis, whilst increasing the efficiency of purification given that H₂O and CO₂ have already been largely removed from the sample. The Giggenbach samples resulted in generally higher ²⁰Ne/²²Ne and ⁴⁰Ar/³⁶Ar ratios compared to the copper tubes samples suggesting that the large amount of gas sampled, coupled with the bottles being pre-evacuated may have resulted in a lower degree of air contamination than the traditional copper tube sampling method. This method also permitted Kr and Xe isotopes to be measured multiple times within the same sample, therefore achieving high precision results (Table S3 and S4; (2)).

³He/⁴He ratios were measured in Giggenbach samples by first taking a 1 cm³ aliquot from the sample bottle. The low-volatility species were trapped onto a series of 3 charcoal cold fingers cooled with liquid N₂ at 77 K for 10 minutes each. The gas was then purified using a Ti-sponge getter at 600°C for 10 minutes to remove any remaining active gas species. Neon was then trapped onto an activated-carbon cryogenic trap held at 50 K. Helium was inlet into a ThermoFisher Scientific® Helix SFT for measurement of the isotopic ratio, taking a sub-aliquot if necessary to reduce signal size to match standards. Neon was then released from the cryogenic trap in order to measure concentrations on a quadrupole mass spectrometer. A charcoal

cold finger was kept at 77 K to minimise $^{40}\text{Ar}^{++}$ interference. Samples were normalised to atmospheric standards run using the same protocol. In this way $^3\text{He}/^4\text{He}$ and $^3\text{He}/^{20}\text{Ne}$ ratios were obtained. The $^3\text{He}/^{22}\text{Ne}$ ratios, as plotted in Figure 2, were then obtained by comparing $^3\text{He}/^{20}\text{Ne}$ ratios with $^{20}\text{Ne}/^{22}\text{Ne}$ ratios measured in the Giggenbachs as described in the following paragraph.

For Ne isotopic analysis, a second 1cm^3 aliquot of gas was expanded in to a different purification line attached to the Helix MC mass spectrometer. The heavy noble gases (Ar, Kr and Xe) were then condensed on to activated charcoal finger held at 77 K for 10 minutes. The remaining He and Ne were then passed through an in-line Ti-sponge getter held at 600°C to remove active gas species. Neon was then trapped on a liquid He cooled cryotrap held at 34 K. Helium remaining in the purification line was then pumped away before Ne was released from the cryotrap at 90 K. The gas was then exposed to a further series of hot (550°C) and cold Ti-sponge getters (50°C) prior to being admitted to the mass spectrometer for analysis. A charcoal cold finger next to the ion source was held at 77 K to minimise the contribution from $^{40}\text{Ar}^{++}$ and CO_2^{++} . Neon isotopes were analysed using peak-jumping over 4 blocks of 15 measurements. All three Ne isotopes were measured on the axial multiplier. The high mass resolution of the Helix MC Plus ($m/\Delta m \approx 1800$) enables the discrimination of the ^{20}Ne peak from $^{40}\text{Ar}^{++}$ (3) and therefore no correction for Ar interference was necessary. The contribution from CO_2^{++} to the ^{22}Ne peak was monitored and corrected for each analysis. Corrections for CO_2^{++} to ^{22}Ne were generally less than 3% on the $^{20}\text{Ne}/^{22}\text{Ne}$ ratio.

The heavy noble gases were then released from the charcoal cold finger at room temperature before being passed through the in-line Ti-sponge getter. Krypton and xenon were recondensed onto a quartz finger held at 77 K. Argon remaining in the line was purified following the same procedure as Ne and admitted to the mass spectrometer for analysis. Argon isotopes were analysed using multi-collection mode, with ^{40}Ar measured on the high mass position (H1) faraday collector, and ^{36}Ar and ^{38}Ar isotopes were measured on the low mass position (L2-CDD) and axial (AX-CDD) compact dynode multiplier, respectively.

Samples with $^{40}\text{Ar}/^{36}\text{Ar}$ values in excess of 1000 (samples 4A and 4B) were chosen for high precision Kr and Xe isotopic analysis. A further 1 cm^3 aliquot of gas was expanded in to the purification line before Kr and Xe were condensed on a quartz finger held at 77 K. The remaining He, Ne and Ar in the line was then pumped away. In order to reduce the partial pressure of Ar remaining in the quartz tube, three dilutions from the quartz tube (20 cm^3) to the whole line ($1,500\text{ cm}^3$) in static mode were made. Krypton and xenon were released from the quartz tube and purified following the same procedure as argon and neon. In order to achieve the highest possible precision and avoid analytical fractionation, Kr and Xe were admitted into the mass spectrometer at the same time, although they were measured on separate aliquots. Krypton and xenon isotopes were measured using peak-jumping mode over 20 cycles, with the amount of gas admitted to the spectrometer being adjusted to fit to that of a standard. During the peak-jumping procedure, the less abundant isotopes of Xe (^{124}Xe , ^{126}Xe , ^{128}Xe) were counted for longer time steps to improve uncertainties (16.8s per cycle for ^{124}Xe , ^{126}Xe , 8.4s for ^{128}Xe compared to 4.2s per

cycle for all other isotopes). A minimum of six repeat analyses were conducted for each sample analysed for Kr and Xe isotopes.

Mass discrimination and sensitivity of the mass spectrometer were determined by the daily analysis of standards of an atmospheric isotopic composition. Uncertainties on the individual repeat analyses correspond to STD/\sqrt{n} , where n is the number of cycles and STD is the standard deviation of the isotopic ratios over the cycles. The final propagated uncertainties include the external errors, which corresponds to long-term reproducibility (standard deviation) of the standards. Uncertainties on the mean represent the standard error (STD/\sqrt{n}) of the repeat analyses. Blanks were significantly less than 1% for all the samples and so no blank correction was applied.

Gases collected in Cu-tubes were transferred to a dedicated extraction and purification line at the University of Oxford, where reactive gases were removed by exposing gases to a titanium sponge held at 950 °C. The titanium sponge was cooled for 15 minutes to room temperature before gases were expanded to a dual hot (SAES GP-50) and cold (SAES NP-10) getter system, held at 250°C and room temperature, respectively. A small aliquot of the gas was segregated for preliminary analysis on a Hiden Analytical HAL-200 quadrupole mass spectrometer. The noble gases were then condensed onto a series of cryogenic traps: the sample was first expanded to an all stainless-steel trap held at an indicative temperature of 15 K. We experimentally established that no Ne or He was trapped under these conditions. Following complete adsorption of Ar, Kr and Xe, the remaining gas was expanded onto a charcoal trap held at 15 K, where He and Ne were quantitatively adsorbed. The temperature on the charcoal finger was then raised to 34 K to release only He,

which was inlet into a Helix SFT mass spectrometer. Following He analysis, the temperature on the charcoal cryogenic trap was raised to 90 K to release Ne, which was inlet into an ARGUS VI mass spectrometer. Following determination of the Ne isotope composition, the stainless steel cryogenic trap temperature was raised to 300 K and a small aliquot of Ar-Kr-Xe was isolated and inlet into the ARGUS VI in order to determine their relative elemental abundances and Ar isotopes. The remaining (>99%) heavy noble gases were then re-adsorbed onto the stainless steel cryogenic trap at 15 K. The temperature was then raised to 200 K for transfer of Kr and Xe to a third cryogenic (charcoal) trap held at 180 K on the preparation line. Following transfer of heavy noble gases, the line was pumped for an additional 15 minutes to remove any residual Ar. The cryogenic trap was then raised to 375 K to ensure complete release of Kr and Xe. Both gases were simultaneously inlet into the ARGUS VI, but only Xe isotopes were analyzed upon the initial expansion. The residual gas remaining in the preparation line was then inlet into the ARGUS VI for simultaneous Kr and Xe isotope determination.

Instrument Performance

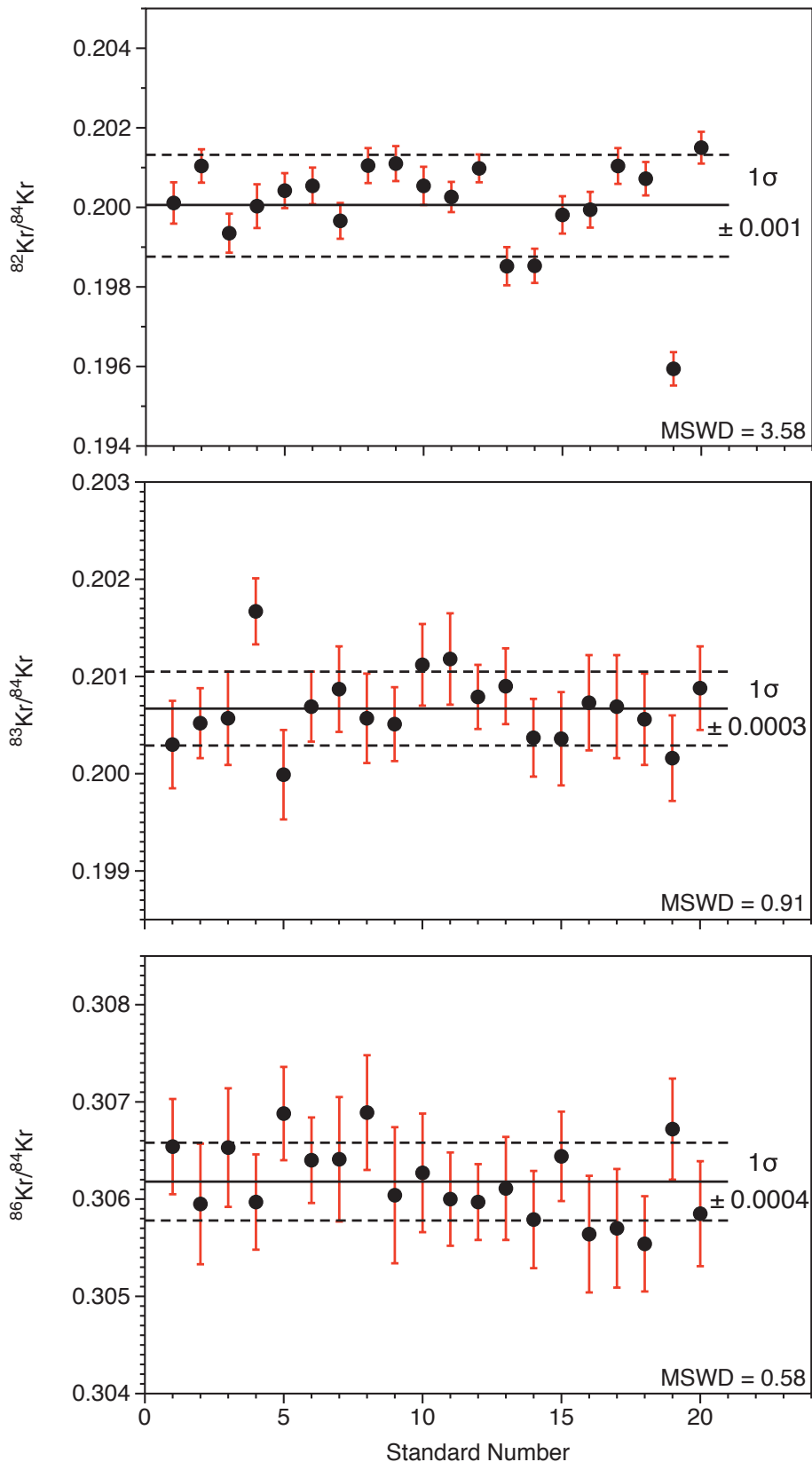


Figure S1. Reproducibility of Kr standard. Standards (n=20) shown here represent all the Kr standards that were analysed during the 3-week period of high precision Kr and Xe analyses conducted on the Brimstone Basin samples. Each standard analysed contains $\sim 1.1 \times 10^{-11}$ moles of ^{84}Kr . Uncertainties on individual measured isotopic ratio correspond to the internal error defined by STD/\sqrt{n} , where n is the

number of cycles (n=20) and STD is the standard deviation on the mean of the isotopic ratio over the cycles. The 1σ error envelope represents the reproducibility of the standard.

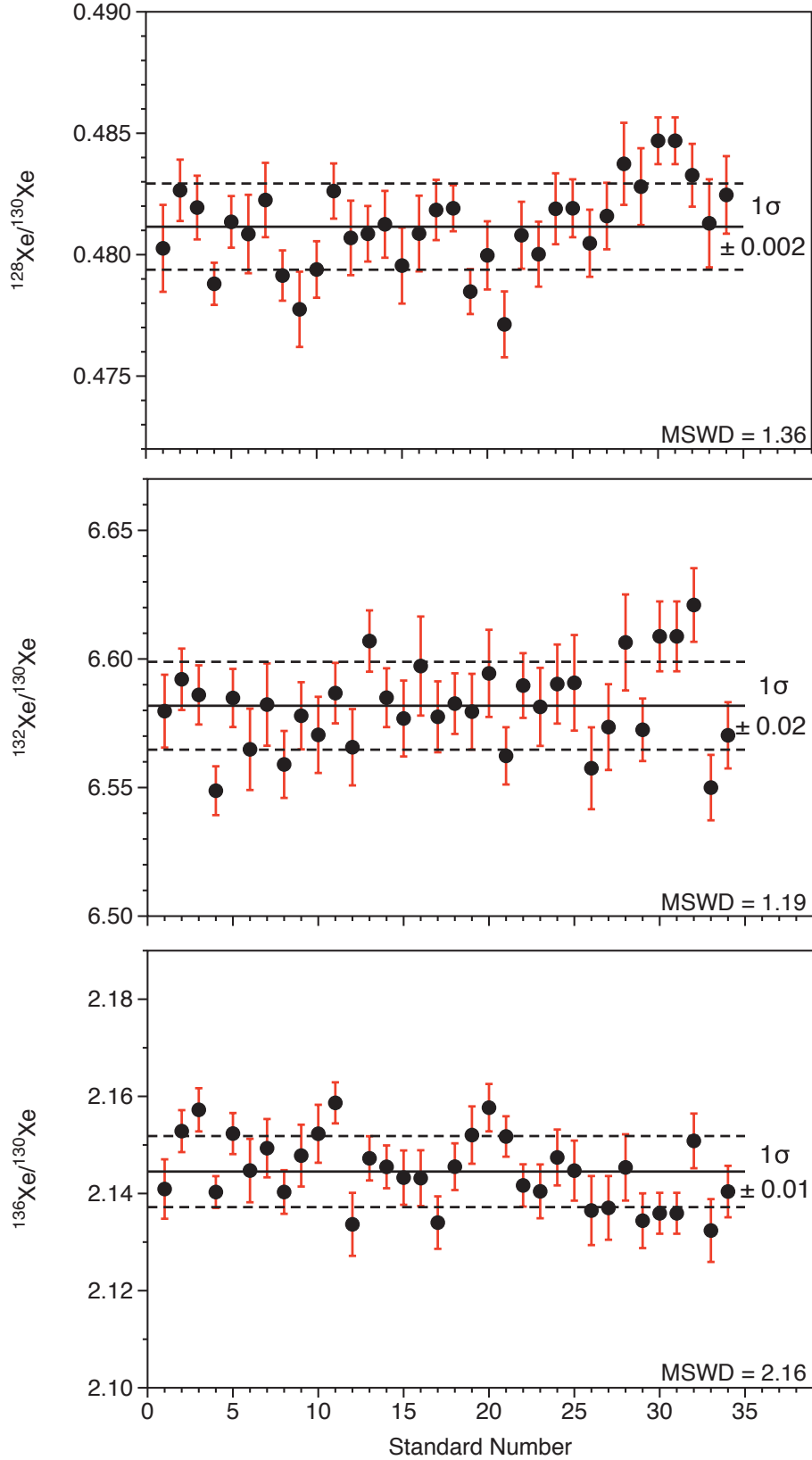


Figure S2. Reproducibility of Xe standard. Standards (n=34) shown here represent all the Xe atmospheric standards that were analysed during the 3-week period of high precision Kr and Xe analyses conducted on the Brimstone Basin samples. Each standard analysed contains $\sim 2.6 \times 10^{-12}$ moles of ^{130}Xe . Uncertainties on individual measured isotopic ratio correspond to the internal error defined by STD/\sqrt{n} , where n is the number of cycles (n=20) and STD is the standard deviation on the mean of the isotopic ratio over the cycles. The 1σ error envelope represents the reproducibility of the standard.

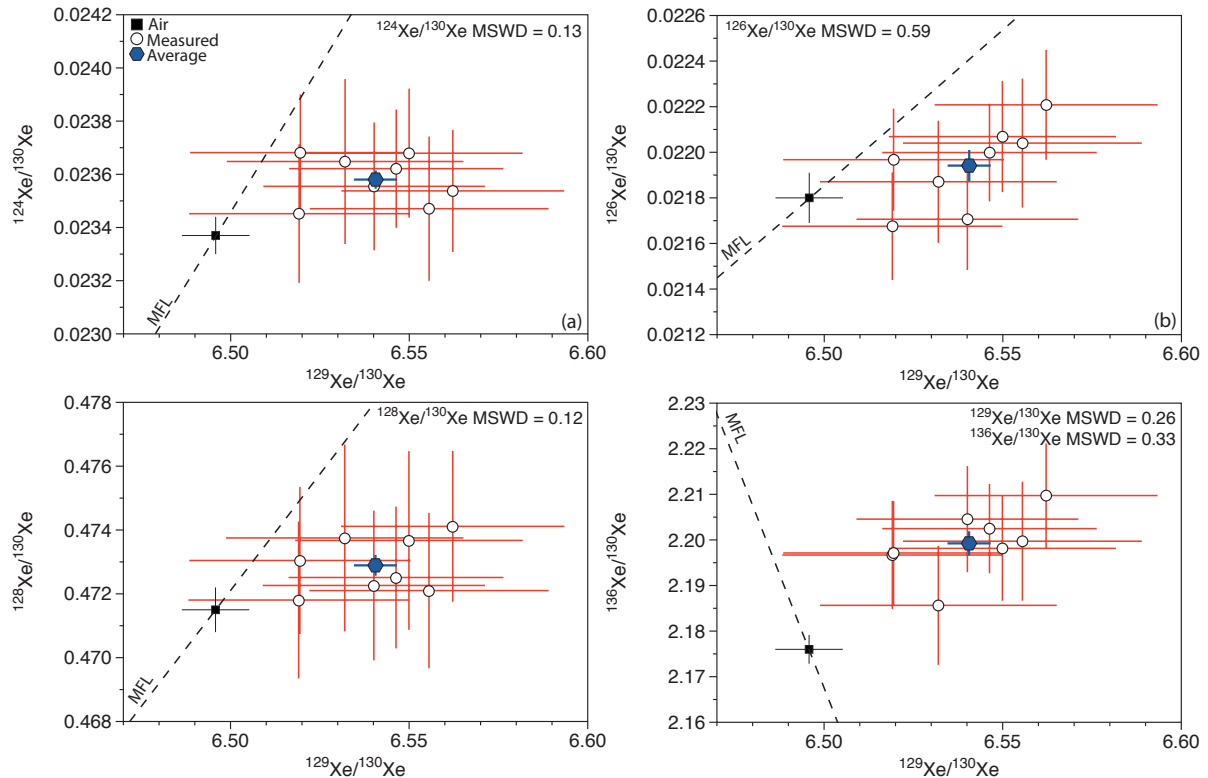


Figure S3. Individual repeat measurements of Xe isotopes in Brimstone Basin sample 4B. The data are shown to be consistently in excess of atmosphere, with the exception $^{126}\text{Xe}/^{130}\text{Xe}$ (b) where two analyses were slightly below atmosphere. The data are randomly distributed and do not follow the mass dependent fractionation line (MFL), ruling out mass fractionation during analysis as the origin of the observed excess in the light Xe isotopes. The mean square weighted deviation (MSWD) for each isotopic ratio is lower than expected (0.46 - 1.53 at 1σ) given the number of repeat measurements (n=8), suggesting that the analytical uncertainties are overestimated (4). The mean of the 8 repeat analyses is shown by the blue hexagon and the uncertainty on the mean represents the standard error ($\text{SE} = \text{STD}/\sqrt{n}$)

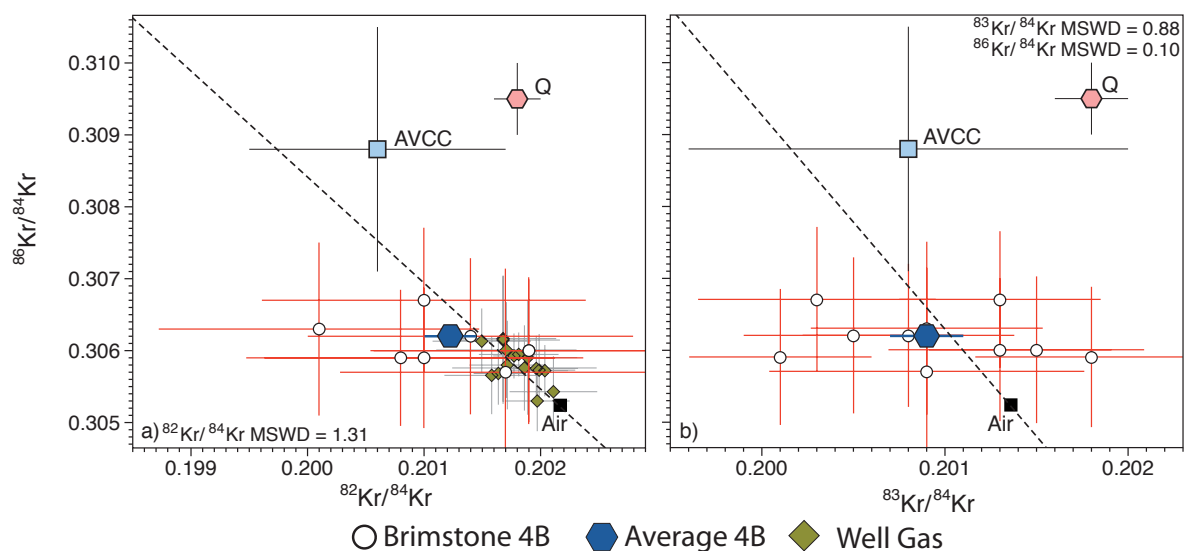


Figure S4. Individual repeat measurements of Kr isotopes in Brimstone Basin sample 4B. The repeat analyses of samples 4B have $^{86}\text{Kr}/^{84}\text{Kr}$ ratios consistently in excess of atmosphere, indicating a chondritic contribution to the Yellowstone mantle source. The average $^{82}\text{Kr}/^{84}\text{Kr}$ (a) and $^{83}\text{Kr}/^{84}\text{Kr}$ (b) ratios suggest the chondritic Kr is similar in composition to AVCC (5), as was previously suggested for upper mantle CO_2 well gases (6). The calculated average $^{82}\text{Kr}/^{84}\text{Kr}$ for sample 4B shown in (a), excludes two repeat analyses, which gave anomalous ^{82}Kr values as a result of the drift of the ^{82}Kr peak during the analysis. This also occurred once during the standard analysis (Figure S1). The data appear randomly distributed and do not follow the mass dependent fractionation line (MFL), suggesting mass fractionation during analysis is not the result in the non-atmospheric signature. Mean square weighted deviation (MSWD) values fall within the expected range (0.53 - 1.47 at 1σ) for uncertainties on individual data points to be representative of the data dispersion given the number of repeat measurements ($n=10$), with the exception of $^{86}\text{Kr}/^{84}\text{Kr}$, which appears to have overestimated uncertainties (4).

Absence of mass-independent isotope fractionation

To ensure that the Ne, Kr and Xe isotopic composition of the Yellowstone magmatic gas is representative of the mantle source, any effect from mass-dependent isotope fractionation must firstly be ruled out. Mass-dependant isotopic fractionation can be inherent to magmatic gas samples (7), or can be induced during sampling, purification and/or analysis. If fractionated atmospheric noble gases were collected during sampling of the Yellowstone magmatic samples, it should be evident for all the noble gas elements.

For example, if $^{20}\text{Ne}/^{22}\text{Ne}$ excesses relative to atmosphere were an artefact mass dependant fractionation, then all noble gas elements should be similarly enriched in light isotopes. To test this hypothesis, we have plotted $^{20}\text{Ne}/^{22}\text{Ne}$ vs. $^{38}\text{Ar}/^{36}\text{Ar}$ together with the expected mass-dependent fractionation lines (Figure S5). The $^{38}\text{Ar}/^{36}\text{Ar}$ of the samples show no significant deviation from atmosphere, despite the variation in $^{20}\text{Ne}/^{22}\text{Ne}$. In addition, the highest $^{20}\text{Ne}/^{22}\text{Ne}$ samples measured in the Giggenbach bottle have atmospheric/mantle-like $^{38}\text{Ar}/^{36}\text{Ar}$ ratios suggesting that the samples do not contain a significant mass-dependently fractionated atmospheric component. Furthermore, Kr is enriched in heavy isotopes relative to atmosphere and would therefore require fractionation to have proceeded in a different direction from Ne and Xe. We therefore conclude that the noble gases within the sample are representative of the mantle source, with little to no fractionated atmosphere being present or introduced to the samples.

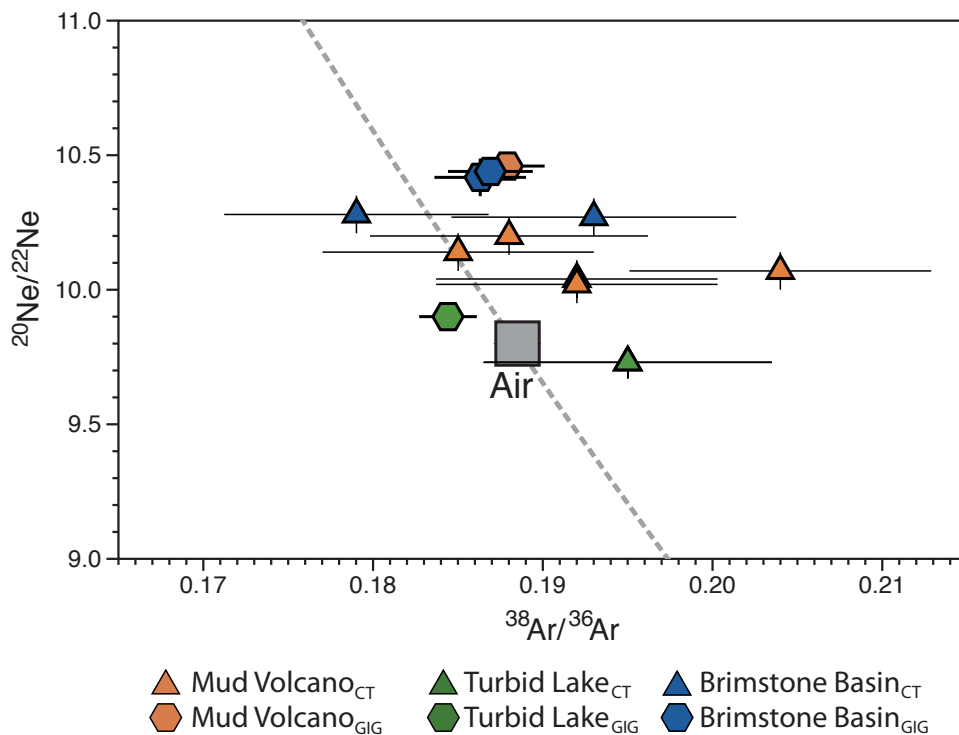


Figure S5. $^{20}\text{Ne}/^{22}\text{Ne}$ vs. $^{38}\text{Ar}/^{36}\text{Ar}$ for all the Yellowstone samples analysed at CRPG and Oxford. The samples do not fall along the mass-dependent fractionation line, instead forming a cluster of data points with variable $^{20}\text{Ne}/^{22}\text{Ne}$ and atmospheric-like $^{38}\text{Ar}/^{36}\text{Ar}$, characteristic of mantle-derived gas. Uncertainties for all samples are shown to 1σ .

Even if a sample shows no evidence of mass-dependent isotope fractionation, it is still possible that light Kr and Xe excesses may be related to fractionation during purification and/or analysis. Nier source mass spectrometers are known to exhibit pressure induced isotopic fractionation (8). As such the amount of Kr and Xe admitted to the mass spectrometer was closely monitored to match that of the standards. Krypton and xenon were purified and analysed following the same procedure, and to therefore explain the apparent mantle-derived Kr and Xe isotopic signature through fractionation would require that Kr and Xe were isotopically depleted and enriched in light isotopes, respectively, which is unlikely. We therefore conclude for a mantle-derived origin of the heavy noble gas anomalies within the Yellowstone samples.

Calculating Mantle Contribution

The contribution of mantle-derived noble gases within the Yellowstone samples was calculated using $^{129}\text{Xe}/^{130}\text{Xe}$, given the unique mantle-derived origin of ^{129}Xe . We firstly assume that the Yellowstone mantle source has a similar composition to that of Iceland (9). This is not an unreasonable assumption given the similarity in $^3\text{He}/^4\text{He}$ (17-20 R_A ; (10)) measured within the modern Icelandic Plume and in Yellowstone ($^3\text{He}/^4\text{He} > 15R_A$; (11, 12)). Taking the $^{129}\text{Xe}/^{130}\text{Xe}$ of the Yellowstone mantle source to be that calculated for the Icelandic plume mantle source (6.98 ± 0.07 ; (9)), we calculate that Yellowstone magmatic gas contains between 7.0 and 12.3% magmatic-derived gas. This takes in to account the complete range of uncertainties

on the $^{129}\text{Xe}/^{130}\text{Xe}$ measured within the Yellowstone magmatic gas (6.541 ± 0.006) and the assumed mantle source composition (6.98 ± 0.07).

Taking the amount of mantle-derived gas calculated from the $^{129}\text{Xe}/^{130}\text{Xe}$, the expected excesses in fissionogenic and non-radiogenic Xe isotope can then be calculated. Firstly, the fissionogenic Xe isotopes are assumed to have an identical composition to the Icelandic mantle source (9). The fissionogenic Xe isotope spectrum calculated from a mantle-air mix of 12.3-87.7% is lower than measured values, due to the presence of fissionogenic Xe from the decay of ^{238}U in the surrounding Archean crust (Figure 3). The composition of light, non-radiogenic Xe isotopes ($^{124,126,128}\text{Xe}$) in the mantle is less well constrained given their relative scarcity and the dominance of recycled atmosphere within the mantle (13). The proportion of primordial Xe in the upper MORB source mantle has been previously estimated to be $22 \pm 13\%$ based on the $^{124}\text{Xe}/^{130}\text{Xe}$ and $^{128}\text{Xe}/^{130}\text{Xe}$ signature measured in MORB popping rocks after correction for atmospheric contamination (14). We independently calculated the atmospheric contribution to the MORB source by extrapolating the light Xe isotope data from several MORB samples (Figure 4; (3, 13, 14)) to the $^{129}\text{Xe}/^{130}\text{Xe}$ MORB mantle endmember (7.6-7.9; (3, 13, 14)). The expected light Xe isotope excesses in Yellowstone samples can therefore be estimated by considering the mantle to be a mix of $23 \pm 10\%$ chondritic Xe, with the remainder being recycled modern atmosphere. The actual measured $^{124}\text{Xe}/^{130}\text{Xe}$, $^{126}\text{Xe}/^{130}\text{Xe}$ and $^{128}\text{Xe}/^{130}\text{Xe}$ ratios in Yellowstone are however higher than would be expected from a source with $23 \pm 10\%$ chondritic Xe, given the excess in $^{129}\text{Xe}/^{130}\text{Xe}$ (Figure 3). This indicates that Yellowstone originates from mantle reservoir with a lower $^{129}\text{Xe}/^{130}\text{Xe}_{\text{Primordial}}$ than MORB.

Correcting for Crustal Input

Samples originating from Brimstone Basin are characterised by low $^3\text{He}/^4\text{He}$ and a high proportion of fissionogenic Xe isotopes, likely contributed from the surrounding Archean-aged crust (12). In order to determine the original magmatic noble gas signature of these gases, it is therefore necessary to correct for this crustal "contamination".

To correct for the production of ^{83}Kr , ^{84}Kr and ^{86}Kr from the fission of ^{238}U , we firstly estimate the amount of excess fission-derived ^{136}Xe within the samples by comparing the measured $^{129}\text{Xe}/^{136}\text{Xe}$ (2.974 ± 0.005) with that of the plume source mantle (2.995 ± 0.003 ; (9)). In this case, the samples would contain a $0.86 \pm 0.26\%$ excess of pure fissionogenic ^{136}Xe . The amount of ^{86}Kr is then calculated using the average $^{136}\text{Xe}/^{86}\text{Kr}$ production ratio (6.45) for the spontaneous fission of ^{238}U (15). The amount of fission-derived ^{83}Kr and ^{84}Kr can then be derived from the $^{83}\text{Kr}/^{86}\text{Kr}$ and $^{84}\text{Kr}/^{86}\text{Kr}$ fission production ratios, respectively (15). The estimated amount of fissionogenic ^{86}Kr within the sample 4B is less than 0.02%, resulting in a minor correction to the $^{82}\text{Kr}/^{84}\text{Kr}$ and $^{86}\text{Kr}/^{84}\text{Kr}$ (Figure S7).

The Ne isotopic signature of Brimstone Basin is also offset from the trend of other sample localities from addition of crustal-derived nucleogenic ^{21}Ne . The amount of crustal ^{21}Ne in the samples can be determined by computing the amount of excess crustal ^4He using the following formula (16):

$$^4\text{He}_{crust} = ^4\text{He}_{total} \times \frac{(^3\text{He}/^4\text{He}_{mantle}) - (^3\text{He}/^4\text{He}_{sample})}{(^3\text{He}/^4\text{He}_{mantle}) - (^3\text{He}/^4\text{He}_{crust})}$$

where the $^3\text{He}/^4\text{He}_{\text{mantle}}$ is taken as the maximum value measured as part of this study ($16.3R_A$), and $^3\text{He}/^4\text{He}_{\text{crust}}$ is taken to be $0.01R_A$ (15). The amount of crustal ^{21}Ne can then be calculated from the crustal $^4\text{He}/^{21}\text{Ne}^*$ production ratio (2.65×10^7 ; (15)). Removing the crustal-derived ^{21}Ne from the Brimstone Basin samples results in them moving back towards the other Yellowstone samples. This correction works well for sample 4B, with the corrected value being within uncertainty of the trend defined by the other Yellowstone samples (Figure S6). However, for sample 4A, it results in an overcorrection testified by the corrected $^{21}\text{Ne}/^{22}\text{Ne}$ value being lower than the atmospheric composition. This may be related to the extremely high $^4\text{He}/^{20}\text{Ne}$ ($> 25,000$) measured within the copper tube of sample 4A in comparison to sample 4B (7,428), with the high ^4He concentration potentially resulting in an overcorrection for crustal ^{21}Ne . If the $^4\text{He}/^{20}\text{Ne}$ measured in the Giggenbach sample from site 4A is used instead to correct the $^{21}\text{Ne}/^{22}\text{Ne}$, then the corrected value is within uncertainty of the corrected sample 4B and overlaps the trend defined by the other Yellowstone samples.

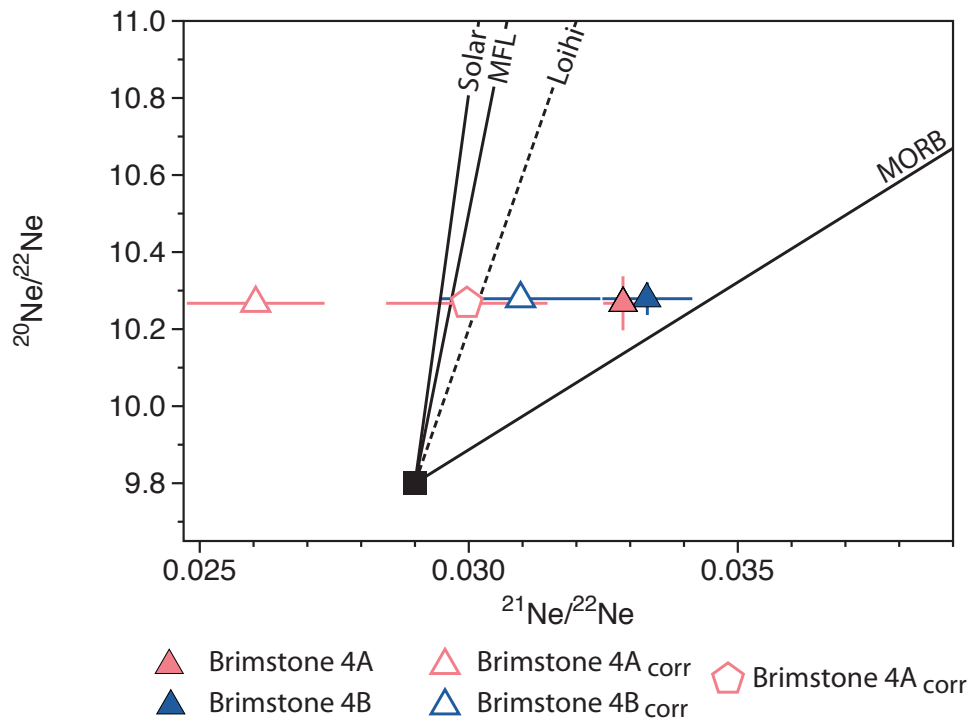


Figure S6. Neon isotopic data for Brimstone Basin corrected for crustal ^{21}Ne addition.

It should be noted that fracture fluids isolated within Precambrian aged crust have been shown to have similar Xe excesses to sample 4B for both the light primordial Xe isotopes and ^{129}Xe , from the retention of ancient atmospheric Xe and the decay of cosmogenic ^{129}I within crustal sediments, respectively (17). An input from a crustal reservoir that has been able to trap ancient atmospheric Xe could therefore also account for the excess measured for the light Xe isotopes and $^{129}\text{Xe}/^{130}\text{Xe}$ relative to atmosphere. We however rule out significant contributions of crustal-derived Xe from the underlying Archean cratonic basement based on the difference in $^{124}\text{Xe}/^4\text{He}$ between sample 4B ($2.04 \pm 0.05 \times 10^{-9}$) and the average Precambrian aged cratonic fluids ($6.8 \pm 1.8 \times 10^{-12}$ SD) (17). The amount of crustal derived noble gases within

sample 4B, as calculated from ^4He , would have brought negligible amounts of ancient trapped atmospheric ^{124}Xe .

The amount of crustal-derived ^{40}Ar can also be determined from the amount of crustal ^4He and the $^4\text{He}/^{40}\text{Ar}$ production ratio of the crust (5.7; (15)). After correcting for crustal-derived ^{40}Ar , the $^{40}\text{Ar}/^{36}\text{Ar}$ of samples 4A and 4B are calculated to be 279 ± 49 and 1001 ± 42 , respectively. Even after correcting for crustal contributions, samples 4B still retains the highest $^{40}\text{Ar}/^{36}\text{Ar}$, further confirming it contains the greatest mantle contribution. The $^{40}\text{Ar}/^{36}\text{Ar}$ of sample 4A is within uncertainty of atmosphere after correction. This suggests that it contains limited amounts of mantle-derived heavy noble gases, or, similarly to the situation for Ne, that the amount of crustal derived ^4He in this sample is overestimated.

Curve Fitting

The Kr and Xe isotopic data from Yellowstone, as well as that from magmatic CO_2 well gases, represent a two-component mixture between mantle-derived gas and the atmosphere. The curvature of mixing hyperbola is defined by $[\text{Xe}/\text{Kr}]_{\text{mantle}}/[\text{Xe}/\text{Kr}]_{\text{Air}}$. Although the $^{130}\text{Xe}/^{84}\text{Kr}$ for air is well defined (0.005; (18)), the mantle composition is less well constrained but has been estimated to have a $^{130}\text{Xe}/^{84}\text{Kr}$ similar to seawater (0.018; (13)). Using these values to determine the curvature of the air-mantle mixing results in a trajectory that does not fit the data from Yellowstone and the Bravo Dome CO_2 well gases (Figure S7). To fit the data, the $[\text{Xe}/\text{Kr}]_{\text{mantle}}/[\text{Xe}/\text{Kr}]_{\text{Air}}$ has to be lower than that produced from published mantle and air $^{130}\text{Xe}/^{84}\text{Kr}$ values.

We determined the $[\text{}^{130}\text{Xe}/\text{}^{84}\text{Kr}]_{\text{mantle}}/[\text{}^{130}\text{Xe}/\text{}^{84}\text{Kr}]_{\text{Air}}$ required to best fit the Yellowstone and Bravo Dome data by performing a total least-square best-fit hyperbolic fit using Matlab. Firstly, the mantle endmember was assumed to have an AVCC-like Kr and Xe isotopic composition (5), and a fixed $^{130}\text{Xe}/\text{}^{84}\text{Kr}$ of 0.018 (13). The Kr and Xe isotopic composition of the atmospheric component was also fixed, whilst the $^{130}\text{Xe}/\text{}^{84}\text{Kr}$ was allowed to freely vary. The $[\text{}^{130}\text{Xe}/\text{}^{84}\text{Kr}]_{\text{mantle}}/[\text{}^{130}\text{Xe}/\text{}^{84}\text{Kr}]_{\text{Air}}$ best able to fit the $^{124}\text{Xe}/\text{}^{130}\text{Xe}$ and $^{126}\text{Xe}/\text{}^{130}\text{Xe}$ data are 0.32 ($\chi^2 = 0.42$) and 0.21 ($\chi^2 = 0.20$), respectively (Figure 6, S7). This is equivalent to the atmospheric component having a $^{130}\text{Xe}/\text{}^{84}\text{Kr}$ of 0.087 and 0.057 as determined from the $^{124}\text{Xe}/\text{}^{130}\text{Xe}$ and $^{126}\text{Xe}/\text{}^{130}\text{Xe}$ data, respectively. The atmospheric component defining the mixing hyperbola is therefore enriched in Xe relative to Kr by 11 to 17 times compared to air. Crustal and hydrothermal fluids, including those sampled in Yellowstone (19), are generally enriched in Xe relative to air. The atmospheric component within the samples may therefore have been introduced during crustal migration rather than during sampling at the surface and/or sampling. Note that all these calculations assume that the mantle $^{130}\text{Xe}/\text{}^{84}\text{Kr}$ is well constrained. However, regardless of the actual mantle values, our results demonstrate that the atmospheric component within Yellowstone and Bravo Dome is 3 to 4 times more enriched in Xe, relative to Kr, than the mantle component (Figure S7).

Supplementary References

1. Y. Sano, T.P Fischer, The analysis and interpretation of noble gases in modern hydrothermal systems. In *The Noble Gases as Geochemical Tracers* (pp. 249-317). Springer, Berlin, Heidelberg (2013).

2. Bekaert, D.V., Broadley, M.W., Caracausi, A. and Marty, B., 2019. Novel insights into the degassing history of Earth's mantle from high precision noble gas analysis of magmatic gas. *Earth and Planetary Science Letters*, **525**, p.115766.
3. M. Honda, Redetermination of the ^{21}Ne relative abundance of the atmosphere, using a high resolution, multi-collector noble gas mass spectrometer (HELIX-MC Plus). *International Journal of Mass Spectrometry*, **387**, pp.1-7 (2015).
4. Wendt, I. and Carl, C., 1991. The statistical distribution of the mean squared weighted deviation. *Chemical Geology: Isotope Geoscience Section*, **86**(4), pp.275-285.
5. R.O. Pepin,. On noble gas processing in the solar accretion disk. *Space Science Reviews*, **106**(1-4), pp.211-230 (2003).
6. G. Holland, M. Cassidy, C.J. Ballentine, Meteorite Kr in Earth's mantle suggests a late accretionary source for the atmosphere. *Science*, **326**(5959), pp.1522-1525 (2009).
7. K. Nagao, N. Takaoka, O. Matsubayashi,. Rare gas isotopic compositions in natural gases of Japan. *Earth Planet Sci Lett*, **53**(2), pp.175-188 (1981).

8. P.G. Burnard, K.A. Farley, Calibration of pressure-dependent sensitivity and discrimination in Nier-type noble gas ion sources. *Geochemistry, Geophysics, Geosystems*, **1**(7) (2000).
9. S. Mukhopadhyay,. Early differentiation and volatile accretion recorded in deep-mantle neon and xenon. *Nature*, **486**(7401), p.101 (2012)
10. D. Harrison, P.G. Burnard, M. Tieloff, G. Turner,. Resolving atmospheric contaminants in mantle noble gas analyses. *Geochemistry, Geophysics, Geosystems*, **4**(3) (2003).
11. H. Craig, J.E. Lupton, J.A. Welhan, R. Poreda, Helium isotope ratios in Yellowstone and Lassen Park volcanic gases. *Geophysical Research Letters*, **5**(11), pp.897-900 (1978)
12. J.B Lowenstern, W.C. Evans, D. Bergfeld, A.G. Hunt, Prodigious degassing of a billion years of accumulated radiogenic helium at Yellowstone. *Nature*, **506** (7488), p.355 (2014).
13. G. Holland, C.J. Ballentine, Seawater subduction controls the heavy noble gas composition of the mantle. *Nature*, **441**(7090), p.186 (2006).
14. S. Péron, M. Moreira, Onset of volatile recycling into the mantle determined by xenon anomalies. *Geochemical Perspective Letters*, **9**, pp.21-25 (2018).

15. C.J. Ballentine, P.G. Burnard, Production, release and transport of noble gases in the continental crust. *Reviews in mineralogy and geochemistry*, **47**(1), pp.481-538 (2002).
16. Ballentine, C.J., Burgess, R. and Marty, B., 2002. Tracing fluid origin, transport and interaction in the crust. *Reviews in mineralogy and geochemistry*, **47**(1), pp.539-614.
17. Holland, G., Lollar, B.S., Li, L., Lacrampe-Couloume, G., Slater, G.F. and Ballentine, C.J., 2013. Deep fracture fluids isolated in the crust since the Precambrian era. *Nature*, **497**(7449), p.357.
18. M. Ozima, F.A. Podosek,. Noble Gas Geochemistry. Cambridge University Press (2002).
19. B.M. Kennedy, M.A. Lynch, J.H. Reynolds, S.P. Smith, Intensive sampling of noble gases in fluids at Yellowstone: I. Early overview of the data; regional patterns. *Geochimica et Cosmochimica Acta*, **49**(5), pp.1251-1261 (1985).
20. M.W. Broadley, R. Burgess, H. Kumagai, N.M. Curran, C.J. Ballentine,. Halogen variations through the quenched margin of a MORB lava: Evidence for direct assimilation of seawater during eruption. *Geochemistry, Geophysics, Geosystems*, **18**(7), pp.2413-2428 (2017).

21. V.S. Heber et al. Noble gas composition of the solar wind as collected by the Genesis mission. *Geochimica et Cosmochimica Acta*, **73**(24), pp.7414-7432 (2009).

22. E. Mazor, D. Heymann, E. Anders, Noble gases in carbonaceous chondrites. *Geochimica et Cosmochimica Acta*, **34**(7), pp.781-824 (1970).

Supplementary Figures

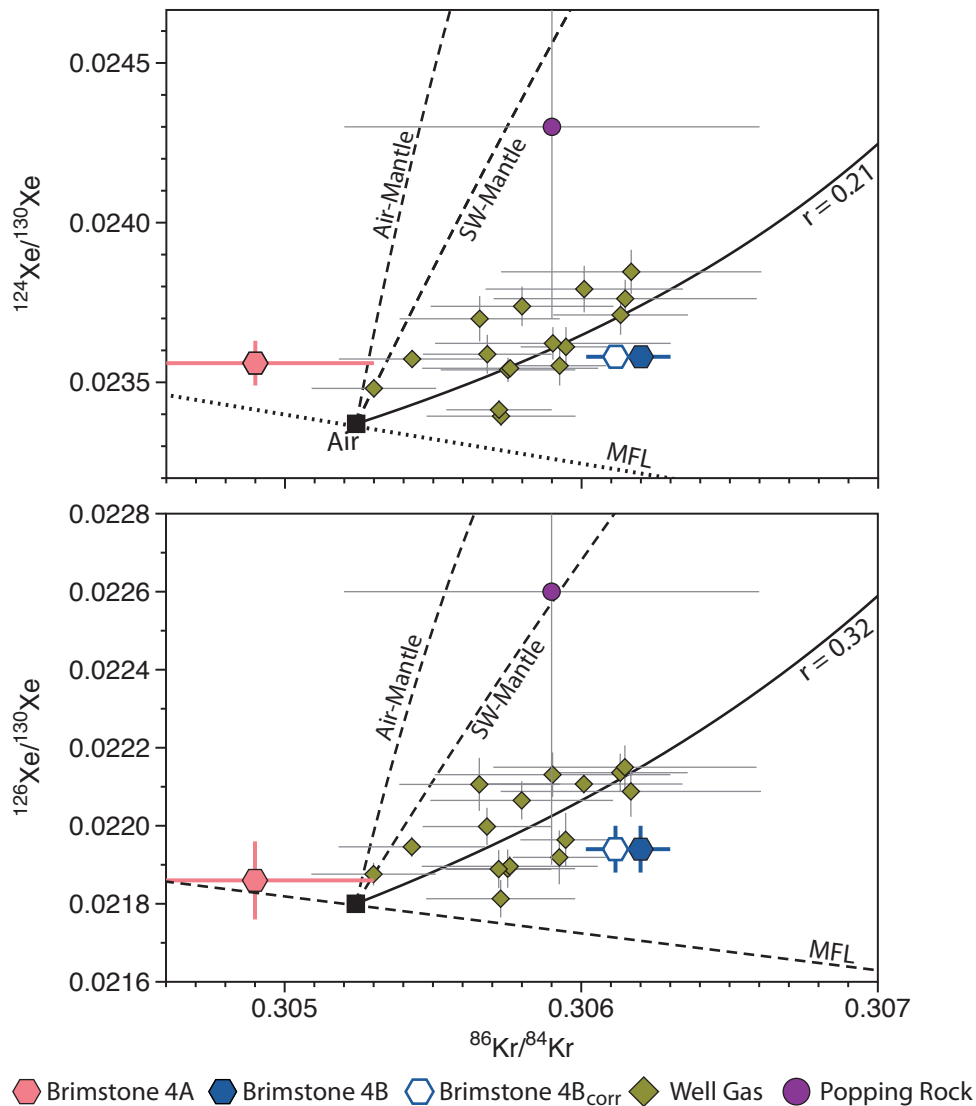


Figure S7. Zoomed in version of Figure 6 in the main text. The Yellowstone samples are shown relative to magmatic CO₂ well gas (6) and MORB popping rock (14). Mixing lines between a chondritic mantle source and potential sources of atmospheric noble gases (atmosphere and seawater) are shown. The MORB popping rock sample lies along the mantle-seawater mixing line, suggesting that seawater may be the source of atmospheric contamination within the basalt (20). Magmatic CO₂ well gases and Yellowstone data define a different trend that requires a Xe-rich atmospheric component, which is potentially related to interaction with Xe-rich crustal fluids. Uncertainties on the Yellowstone and Well Gas data represent 1SE (Standard Error).

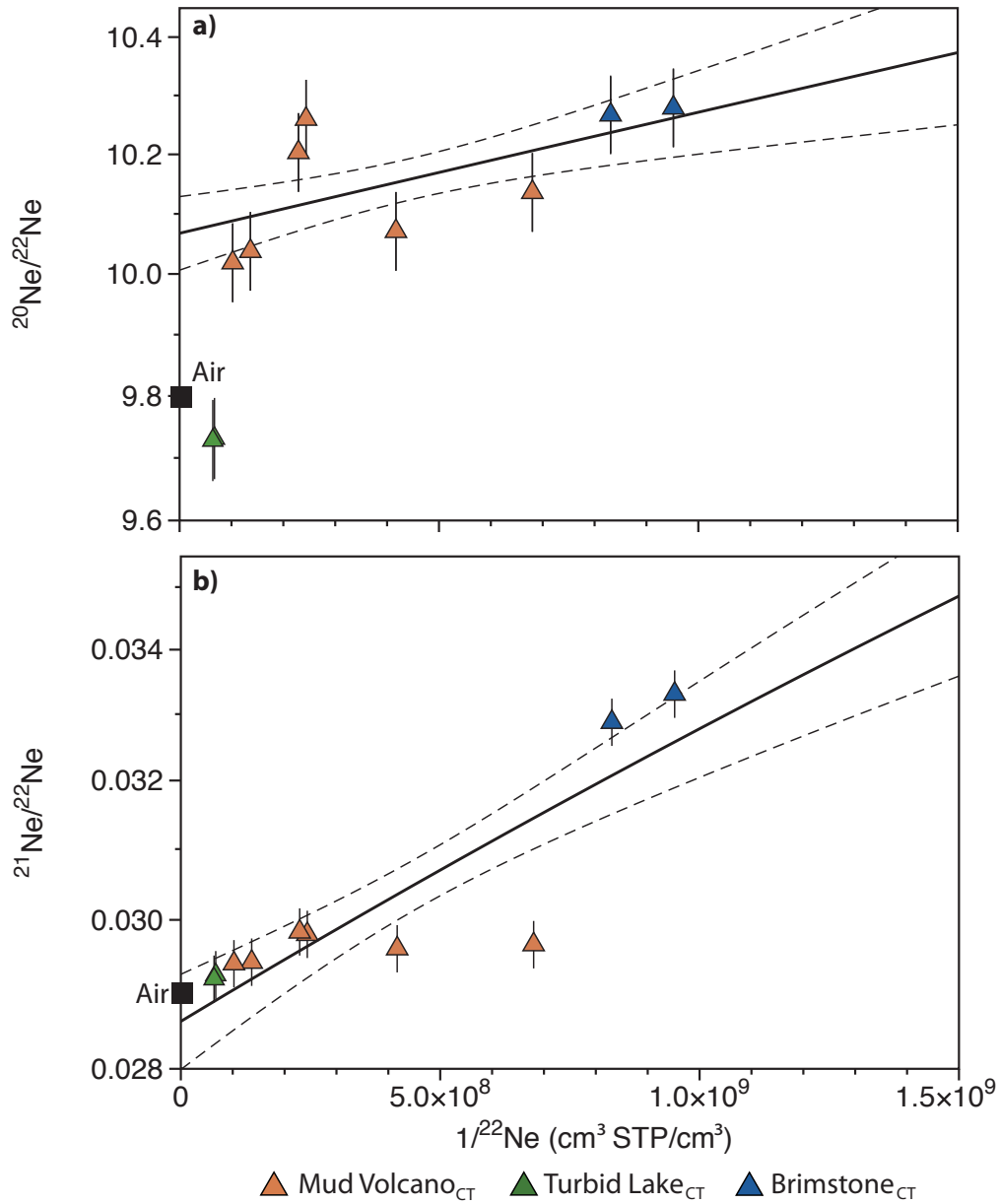


Figure S8. $^{20}\text{Ne}/^{22}\text{Ne}$ (a) and $^{21}\text{Ne}/^{22}\text{Ne}$ (b) plotted relative to inverse ^{22}Ne concentrations. Samples in excess of atmosphere and therefore containing mantle-derived Ne fall along the same trend, suggesting that all sites originate from a similar mantle source.

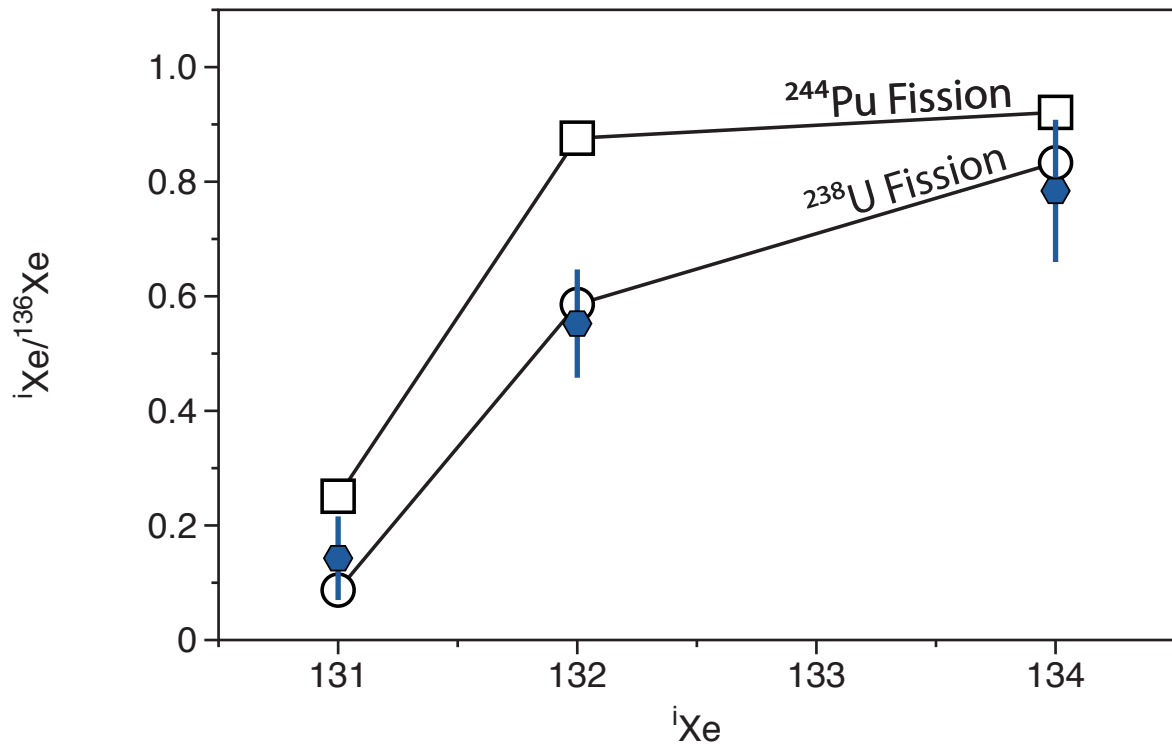


Figure S9. Fission spectrum of Brimstone Basin samples 4B. The excess in $^{131-136}\text{Xe}$ of sample 4B is compared to the fission spectra of ^{238}U and ^{244}Pu . The sample best fit the ^{238}U spectra, suggesting that crustal-derived Xe dominates the signature of the fissionogenic Xe isotopes in Yellowstone samples. Uncertainties for the Yellowstone samples are shown to 1SE.

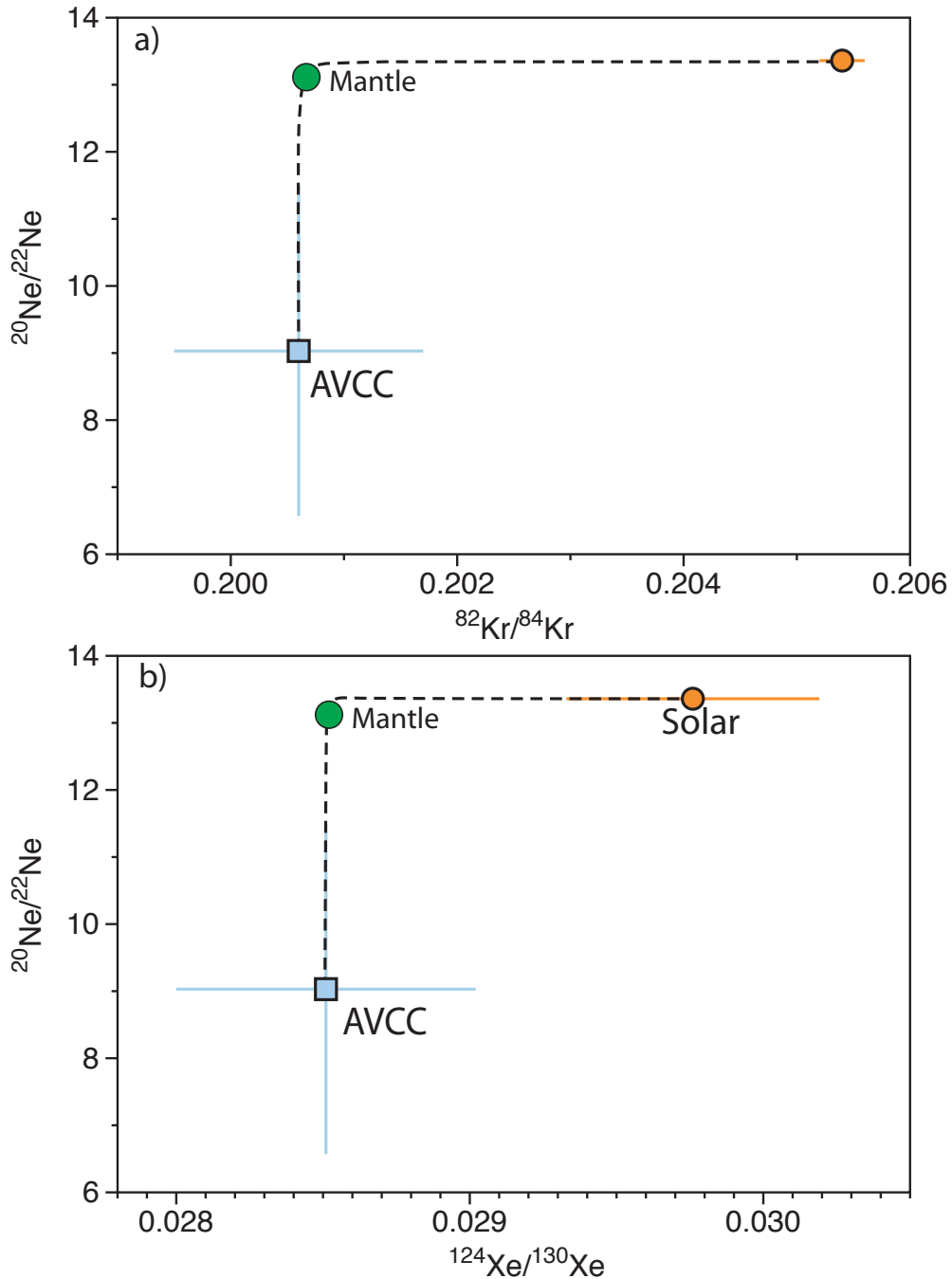


Figure S10. Mixing of solar and chondritic Kr (a) and Xe (b) in the Earth's mantle. The curvature of the mixing lines are defined by the $[\text{Ne}/\text{Kr}]_{\text{solar}}/[\text{Ne}/\text{Kr}]_{\text{chondritic}}$ and $[\text{Ne}/\text{Xe}]_{\text{solar}}/[\text{Ne}/\text{Xe}]_{\text{chondritic}}$ for figure (a) and (b), respectively. The large differences between the solar $^{22}\text{Ne}/^{84}\text{Kr}$ (7508 ± 477) and $^{22}\text{Ne}/^{130}\text{Xe}$ ($4.3 \pm 0.5 \times 10^5$) (21), and those of chondrites ($^{22}\text{Ne}/^{84}\text{Kr} \approx 4.6$, $^{22}\text{Ne}/^{130}\text{Xe} \approx 39.6$) (22), enable nebular ingassing to dominate the Earth's mantle Ne signature without significantly changing the Kr and Xe isotopic signatures. Due to the extreme curvature of mixing, changing the chondritic Ne end-member from CI-chondrites to Ne-B, or replacing elemental ratios from chondritic to those currently measured in the mantle, would not result in any significant change to our estimations.

Table S1. Noble gas concentrations of Yellowstone gas samples measured within copper tubes.

Sample	Location	Coordinates	⁴ He cm ³		²⁰ Ne cm ³		⁴⁰ Ar cm ³		⁸⁴ Kr cm ³		¹³² Xe cm ³	
			STP/cm ³	±	STP/cm ³	±	STP/cm ³	±	STP/cm ³	±	STP/cm ³	±
1A	Mud Volcano	44.62487 -110.43306	1.97E-05	5.29E-07	7.35E-08	2.97E-10	9.95E-05	2.29E-06	7.86E-09	2.97E-11	6.84E-10	2.37E-12
1Ab	Mud Volcano	44.62487 -110.43306	1.73E-05	4.64E-07	9.79E-08	3.96E-10	1.09E-04	2.50E-06	1.04E-08	3.94E-11	9.25E-10	3.21E-12
1B	Mud Volcano	44.62487 -110.43306	1.14E-05	3.04E-07	1.49E-08	6.03E-11	2.92E-05	6.72E-07	1.86E-09	7.03E-12	1.32E-10	4.57E-13
1Bb	Mud Volcano	44.62487 -110.43306	1.59E-05	4.27E-07	2.41E-08	9.77E-11	3.76E-05	8.66E-07	2.75E-09	1.04E-11	1.98E-10	6.84E-13
2A	Mud Volcano	44.62315 -110.43195	1.73E-05	4.64E-07	4.45E-08	1.80E-10	5.46E-05	1.26E-06	4.11E-09	1.55E-11	2.81E-10	9.75E-13
3C	Turbid Lake	44.54664 -110.26041	3.23E-04	8.64E-06	1.45E-07	5.85E-10	3.44E-04	7.93E-06	3.47E-08	1.31E-10	2.95E-09	1.02E-11
3Cb	Turbid Lake	44.54664 -110.26041	1.16E-04	3.10E-06	1.52E-07	6.14E-10	2.86E-04	6.59E-06	3.27E-08	1.24E-10	2.86E-09	9.92E-12
4A	Brimstone Basin	44.38841 -110.21889	2.71E-04	7.27E-06	1.24E-08	5.00E-11	4.80E-05	1.11E-06	7.44E-10	2.81E-12	4.63E-11	1.60E-13
4B	Brimstone Basin	44.38700 -110.21915	8.02E-05	2.15E-06	1.08E-08	4.37E-11	4.02E-05	9.26E-07	7.30E-10	2.76E-12	4.62E-11	1.60E-13

0 Uncertainties are reported to 1σ.

1

2

3

4

5

6 **Table S2.** Helium, neon and argon isotopic composition of Yellowstone volcanic gas samples

	Location	$^3\text{He}/^4\text{He}$ (R/R _A)	±	$^{20}\text{Ne}/^{22}\text{Ne}$	±	$^{21}\text{Ne}/^{22}\text{Ne}$	±	$^{40}\text{Ar}/^{36}\text{Ar}$	±	$^{38}\text{Ar}/^{36}\text{Ar}$	±	$^3\text{He}/^{22}\text{Ne}$	±
1A	Mud Volcano	14.42	0.90	10.04	0.07	0.0294	0.0003	346.0	7.0	0.1920	0.0083	0.054	0.004
1Ab	Mud Volcano	13.12	0.82	10.02	0.07	0.0294	0.0003	350.2	7.0	0.1920	0.0083	0.033	0.002
1B	Mud Volcano	13.17	0.82	10.14	0.07	0.0297	0.0003	469.2	9.5	0.1850	0.0080	0.142	0.010
<i>1B (Gig)</i>	Mud Volcano	<i>16.26</i>	<i>0.03</i>	<i>10.46</i>	<i>0.05</i>	<i>0.0306</i>	<i>0.0004</i>	<i>373.2</i>	<i>1.7</i>	<i>0.1879</i>	<i>0.0022</i>	<i>0.146</i>	<i>0.007</i>
1Bb	Mud Volcano	14.45	0.90	10.07	0.07	0.0296	0.0003	525.2	10.6	0.2040	0.0089	0.134	0.009
2A	Mud Volcano	13.81	0.86	10.20	0.07	0.0298	0.0003	414.1	8.3	0.1880	0.0082	0.077	0.005
3C	Turbid Lake	2.26	0.14	9.73	0.06	0.0292	0.0003	340.3	7.1	0.1950	0.0085	0.069	0.005
<i>3C (Gig)</i>	Turbid Lake	<i>2.86</i>	<i>0.03</i>	<i>9.90</i>	<i>0.03</i>	<i>0.0296</i>	<i>0.0006</i>	<i>394.9</i>	<i>1.1</i>	<i>0.1844</i>	<i>0.0017</i>	<i>0.000021</i>	<i>0.000001</i>
3Cb	Turbid Lake	2.18	0.14	9.73	0.06	0.0292	0.0003	339.5	6.8	0.1950	0.0085	0.023	0.002
4A	Brimstone Basin	2.52	0.16	10.27	0.07	0.0329	0.0004	1536.4	31.0	0.1930	0.0084	0.794	0.054
<i>4A (Gig)</i>	Brimstone Basin	<i>3.04</i>	<i>0.10</i>	<i>10.42</i>	<i>0.07</i>	<i>0.0362</i>	<i>0.0005</i>	<i>1589.7</i>	<i>7.1</i>	<i>0.1863</i>	<i>0.0027</i>	<i>0.193</i>	<i>0.026</i>
4B	Brimstone Basin	2.34	0.15	10.28	0.07	0.0333	0.0004	1417.1	28.5	0.1790	0.0078	0.250	0.017
<i>4B (Gig)</i>	Brimstone Basin	<i>3.02</i>	<i>0.03</i>	<i>10.44</i>	<i>0.04</i>	<i>0.0356</i>	<i>0.0008</i>	<i>1485.5</i>	<i>6.2</i>	<i>0.1869</i>	<i>0.0025</i>	<i>0.216</i>	<i>0.046</i>

7 Samples collected in Giggenbach bottles are in italics. Uncertainties are reported to 1σ.

8 **Table S3.** Xenon isotopic composition of gas collected in Giggenbach bottles from Brimstone Basin.

	$^{124}\text{Xe}/^{130}\text{Xe}$	\pm	$^{126}\text{Xe}/^{130}\text{Xe}$	\pm	$^{128}\text{Xe}/^{130}\text{Xe}$	\pm	$^{129}\text{Xe}/^{130}\text{Xe}$	\pm	$^{131}\text{Xe}/^{130}\text{Xe}$	\pm	$^{132}\text{Xe}/^{130}\text{Xe}$	\pm	$^{134}\text{Xe}/^{130}\text{Xe}$	\pm	$^{136}\text{Xe}/^{130}\text{Xe}$	\pm
4A																
#1	0.02351	0.00022	0.02172	0.00022	0.4723	0.0021	6.490	0.030	5.180	0.017	6.579	0.022	2.568	0.010	2.188	0.009
#2	0.02349	0.00025	0.02222	0.00025	0.4741	0.0021	6.543	0.032	5.210	0.021	6.627	0.022	2.582	0.011	2.196	0.010
#3	0.02382	0.00027	0.02186	0.00025	0.4741	0.0022	6.529	0.032	5.208	0.020	6.606	0.022	2.573	0.011	2.187	0.010
#4	0.02344	0.00025	0.02202	0.00023	0.4740	0.0022	6.528	0.032	5.210	0.020	6.613	0.022	2.576	0.010	2.195	0.009
#5	0.02372	0.00026	0.02147	0.00023	0.4718	0.0023	6.492	0.031	5.178	0.020	6.575	0.021	2.563	0.010	2.173	0.009
#6	0.02338	0.00024	0.02189	0.00023	0.4731	0.0024	6.519	0.032	5.197	0.020	6.608	0.023	2.568	0.011	2.184	0.010
Average	0.02356	0.00007	0.02186	0.0001	0.4732	0.0004	6.517	0.009	5.197	0.006	6.601	0.008	2.572	0.003	2.187	0.003
4B																
#1	0.02362	0.00022	0.02200	0.00021	0.4725	0.0022	6.546	0.030	5.220	0.019	6.610	0.021	2.587	0.010	2.202	0.010
#2	0.02355	0.00024	0.02171	0.00022	0.4722	0.0023	6.540	0.031	5.205	0.019	6.626	0.024	2.573	0.011	2.205	0.012
#3	0.02354	0.00023	0.02221	0.00024	0.4741	0.0024	6.562	0.031	5.238	0.020	6.637	0.023	2.588	0.010	2.210	0.011
#4	0.02345	0.00026	0.02168	0.00024	0.4718	0.0025	6.519	0.031	5.202	0.019	6.583	0.023	2.568	0.010	2.197	0.012
#5	0.02368	0.00022	0.02197	0.00022	0.4730	0.0023	6.519	0.031	5.216	0.019	6.619	0.021	2.582	0.010	2.197	0.011
#6	0.02347	0.00027	0.02204	0.00028	0.4721	0.0024	6.556	0.033	5.218	0.021	6.622	0.026	2.585	0.012	2.200	0.013
#7	0.02368	0.00024	0.02207	0.00024	0.4737	0.0028	6.550	0.032	5.217	0.019	6.635	0.023	2.584	0.009	2.198	0.011
#8	0.02365	0.00030	0.02187	0.00027	0.4737	0.0029	6.532	0.033	5.214	0.020	6.628	0.027	2.583	0.012	2.186	0.013
Average	0.02358	0.00003	0.02194	0.00006	0.4729	0.0003	6.541	0.006	5.216	0.004	6.620	0.006	2.581	0.003	2.199	0.002
Standard	0.02483	0.00018	0.02286	0.00015	0.4812	0.0018	6.480	0.026	5.171	0.013	6.582	0.017	2.537	0.007	2.145	0.007
Atmosphere	0.02337		0.02180		0.4715		6.496		5.213		6.607		2.563		2.176	

9

10 Uncertainty on the mean represents STD/\sqrt{n} . Each measured isotopic ratio represents the mean of the ratio analysed over 20

11 analytical cycles. The uncertainties for the individual repeat analyses corresponds to STD/\sqrt{n} , where n is the number of cycles (20)

12 and STD is the standard deviation of the isotopic ratios over the 20 cycles. Final uncertainties are propagated to include the
13 external errors, which corresponds to long-term reproducibility (standard deviation) over 34 standards. The average and standard
14 deviation of 34 standards (not normalised to atmosphere) are also shown. Atmospheric values are from ref [18](#).

15 **Table S4.** Krypton isotopic composition of gas collected in Giggenbach bottles from Brimstone Basin, not corrected for fission
 16 contributions.

	$^{82}\text{Kr}/^{84}\text{Kr}$	\pm	$^{83}\text{Kr}/^{84}\text{Kr}$	\pm	$^{86}\text{Kr}/^{84}\text{Kr}$	\pm
4A						
#1	0.1984	0.0013	0.2010	0.0006	0.3048	0.0007
#2	0.2024	0.0013	0.2010	0.0006	0.3059	0.0006
#3	0.1969	0.0013	0.2006	0.0006	0.3030	0.0007
#4	0.2019	0.0013	0.2014	0.0007	0.3048	0.0008
#5	0.1936	0.0012	0.1989	0.0006	0.3059	0.0007
#6	0.2006	0.0014	0.2016	0.0005	0.3048	0.0006
Average	0.1990	0.0014	0.2008	0.0004	0.3049	0.0004
4B						
#1	0.2010	0.0014	0.2018	0.0006	0.3059	0.0010
#2	0.2017	0.0014	0.2009	0.0009	0.3057	0.0014
#3*	0.1958	0.0013	0.2013	0.0006	0.3067	0.0009
#4	0.2001	0.0014	0.2009	0.0006	0.3063	0.0012
#5*	0.1970	0.0013	0.2008	0.0006	0.3062	0.0010
#6	0.2014	0.0014	0.2005	0.0006	0.3062	0.0011
#7	0.2008	0.0013	0.2001	0.0005	0.3059	0.0009
#8	0.2019	0.0014	0.2013	0.0006	0.3060	0.0010
#9	0.2010	0.0014	0.2003	0.0006	0.3067	0.0010
#10	0.2019	0.0013	0.2015	0.0006	0.3060	0.0010
Average	0.2012	0.0002	0.2009	0.0002	0.3062	0.0001
Standard	0.2001	0.0013	0.2007	0.0003	0.3062	0.0004
Atmosphere	0.2022		0.2014		0.3052	

17

18 Uncertainty on the mean represents STD/\sqrt{n} . Each measured isotopic ratio represents the mean of the ratio analysed over 20
19 analytical cycles. The uncertainties for the individual repeat analyses correspond to STD/\sqrt{n} , where n is the number of cycles (20)
20 and STD is the standard deviation of the isotopic ratios over the 20 cycles. Final uncertainties are propagated to include the
21 external errors, which corresponds to long-term reproducibility (standard deviation) over 20 standards. * Signifies repeat analyses of
22 samples 4B that have anomalous $^{82}\text{Kr}/^{84}\text{Kr}$ relative to the average, resulting from instrument drift on the ^{82}Kr peak during the
23 analysis (Figure S4). These repeat analyses are not included in the average. The average and standard deviation of 20 standards
24 (not normalised to atmosphere) are also shown. Atmospheric values are from ref [18](#).

25